Physical mechanism of centrifugal-gravity wave resonant instability in azimuthally symmetric swirling flows

Ron Yellin-Bergovoy,[1,*] Eyal Heifetz,[1] and Orkan M. Umurhan[2]
[1]*Department of Geophysics, School of Earth Sciences, Tel-Aviv University, Tel-Aviv, Israel*
[2]*NASA Ames Research Center, Division of Space Sciences, Planetary Systems Branch, Moffett Field, California 94035, USA*
(Received 6 February 2017; published 11 October 2017)

We present an explicit analysis of wave-resonant instability of swirling flows inside fast rotating cylindrical containers. The linear dynamics are decomposed into the interaction between the horizontal inner centrifugal edge waves and the outer vertical gravity waves with the aim of understanding the dynamics of the centrifugal waves. We show how the far field velocity induced respectively by the centrifugal and the gravity waves affect each other's propagation rates and amplitude growth. We follow this with an analysis of the instability in terms of a four-wave interaction, two centrifugal and two gravity ones, and explain why the resonant instability can be obtained only between a pair of two counterpropagating waves, one centrifugal and one gravity. Furthermore, a near resonant regime which does not yield instability is shown to result from a phase-locking configuration between a pair of a counterpropagating centrifugal wave and a propropagating gravity one, where the interaction affects the waves' propagation rates but not the amplitude growth.

DOI: 10.1103/PhysRevFluids.2.104801

I. INTRODUCTION

The emergence of steady polygonal patterns in swirling flows inside rotating cylindrical containers is both beautiful and intriguing [1–11]. In the experiments, a cylindrical container is filled with liquid (usually water) and the bottom plate is rotated while the cylinder remains at rest. Recent work [12–15] has shown that at high rotation rates the mean flow rotates approximately as an irrotational vortex (denoted by Fabre and Mougeul [13], hereafter FM14, as the "Dry Potential" regime). In this regime the wave instability results mainly from resonant interaction between vertical-azimuthal gravity waves on the outer perimeter of the cylinder (at the top of the flow) and centrifugal horizontal-azimuthal waves on the cylinder surface, at the inner interface between the flow and the air (Fig. 1). Tophøj *et al.*) [15], hereafter TMBF, employed the potential flow theory to simplify the dynamics and showed that their analysis captures the essence of the dynamics, a fact that has been confirmed by FM14. A theory of the fully developed polygonal states, in terms of traveling cnoidal waves, has been presented by Ref. [16]. By independently controlling the rotation rates of the bottom plate and the cylinder [11], the apparatus could move from a Newton's bucket state, where the fluid is at rest in the rotating frame, to a state where the rotation rate of the fluid is minimal and the shear rate is maximal, which is reflected by an almost flat surface and strong turbulence. In between these two extreme cases they found polygonal states for which the rotational symmetry is spontaneously broken.

As a tangent to that, a growing body of literature is devoted to understanding various scenarios of shear instability in terms of interaction-at-a-distance between counterpropagating interfacial vorticity waves (e.g., Refs. [17–21]). In brief, the idea behind this way of thinking is that the phase relation between the wave's vorticity and displacement determines the direction of the wave propagation in isolation. In the presence of shear, flow two interfacial waves with an oppositely signed vorticity-displacement relationship may remain phase-locked to each other if each wave propagates counter its local mean flow (viewed from the frame of reference of the averaged mean flow). By implementing vorticity inversion, that is, by obtaining the velocity far field induced by the

*yellinr@post.tau.ac.il

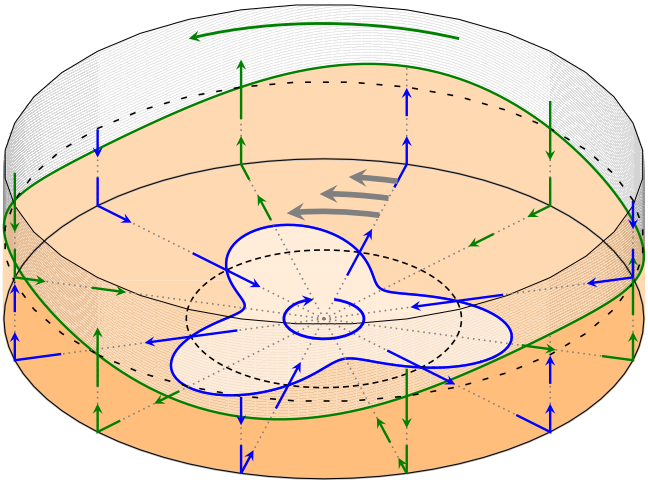

FIG. 1. Resonant interaction between counterpropagating gravity wave (green), and a counterpropagating centrifugal wave (blue). The green and blue azimuthal arrows represent the waves direction of propagation, and the radial (vertical) arrows indicate the induced velocity field by each wave. The gray thick arrows illustrate the basic state flow velocity ($\bar{V} \propto \frac{1}{r}$), and the black dashed lines show the interfaces of the unperturbed mean flow. The white polygon in the middle of the cylinder represents the "dry patch" of the vortex.

interfacial vorticity waves, one can formulate how each wave pushes the displacement of the other further. If the counterpropagating waves are phase-locked, this mutual amplification sustains and thus enables resonance instability. For more details on this physical scenario the reader is referred to the review paper [22].

Here we wish to implement this wave action at-a-distance concept to the free surface swirling flow, while keeping the potential flow formulation of TMBF. As we will see, this analysis sheds light both on the nature of the inner horizontal centrifugal waves as well as on the resonant mechanism between the latter and the vertical gravity waves at the outer circumference of the cylinder.

The rest of the paper is organized as follows. In Sec. II we formulate the problem setup and linearize the equations with respect to the mean flow. In Sec. III we investigate the propagation mechanism of the waves in isolation, where in Sec. IV we write the explicit wave interaction equations and solve them for the resonance condition. We end by discussing our results and routes for future work.

II. FORMULATION

A. Setup

We refer to a laboratory experiment in which a cylindrical container is filled to a certain height H with an incompressible fluid and the bottom plate is rotated while the cylinder remains at rest (Fig. 2); see, e.g., Ref. [11]. We limit the analysis to the "Dry Potential" regime where the equilibrium state of the fluid can be approximated as an irrotational vortex, as suggested by TMBF. We consider therefore a potential flow where the governing momentum equations in the radial (r), azimuthal (θ), and height (z) coordinates for the respective $\mathbf{v} = (u, v, w)$ velocity components can be written in the inertial frame as

$$\frac{Du}{Dt} = \frac{v^2}{r} - \frac{1}{\rho}\frac{\partial p}{\partial r}, \tag{1}$$

$$\frac{Dv}{Dt} = -\frac{uv}{r} - \frac{1}{\rho r}\frac{\partial p}{\partial \theta}, \tag{2}$$

$$\frac{Dw}{Dt} = -g - \frac{1}{\rho}\frac{\partial p}{\partial z}. \tag{3}$$

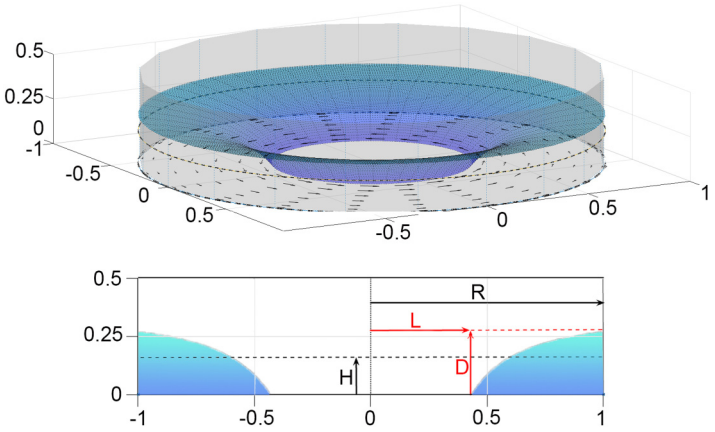

FIG. 2. Side view (top) and radial-vertical cross section (bottom) of the unperturbed equilibrium flow in a state of an irrotational vortex, scaled by the cylinder radius R. H is the fluid height at rest, D is the maximum height of the rotated flow, and L is its inner radius.

Here the constant density is ρ, p is the pressure, g is gravity, and t denotes time. The material derivative is $\frac{D}{Dt} \equiv \frac{\partial}{\partial t} + u\frac{\partial}{\partial r} + \frac{v}{r}\frac{\partial}{\partial \theta} + w\frac{\partial}{\partial z}$. Following TMBF we assume that the azimuthally independent unperturbed equilibrium flow (denoted by overbars) is an irrotational vortex with circulation Γ, sketched in Fig. 2:

$$\overline{U} = 0\,, \quad \overline{V} = \overline{\Omega} r = \frac{\Gamma}{2\pi r}\,, \quad \overline{W} = 0. \tag{4}$$

Substituting the mean flow solution into the momentum equations (1)–(3) yields the partial differential equations governing the unperturbed pressure gradient force:

$$\frac{1}{\rho}\frac{\partial}{\partial r}\overline{P}(r,z) = \frac{\overline{V}^2}{r} = \overline{\Omega}^2 r\,, \quad \frac{1}{\rho}\frac{\partial}{\partial z}\overline{P}(r,z) = -g. \tag{5}$$

Since the pressure is constant on the free surface of the flow, the surface height Z_s satisfies

$$\frac{Z_s(r)}{H} = \frac{F^2}{2}\left[\left(\frac{R}{L}\right)^2 - \left(\frac{R}{r}\right)^2\right], \tag{6}$$

where L and R are respectively the inner and outer radii of the irrotational vortex and the subscript s denotes the free surface. H is the fluid height at rest, and

$$F^2 = \frac{\overline{V}^2(R)}{gH} \tag{7}$$

is the square of the Froude number for this setup. We note that $F = F_p/\sqrt{A}$, where $F_p \equiv \Omega(R)\sqrt{R/g}$ is the "plate" Froude number, as defined by FM14, and $A = H/R$ is the aspect ratio of the fluid at rest. Mass conservation implies as well that $D = Z_s(R)$ satisfies

$$\frac{D}{H} = 1 + F^2 \ln\left(\frac{R}{L}\right). \tag{8}$$

Equating (6) with (8) for $r = R$, with the aid of (4), gives expressions for F, Γ, and D in terms of (H, R, L) (see TMBP for more details; note, however, the different notation). FM14 showed that for $F_p > 2.5$ and $A = 0.3$, that is, for $F > 5$, the potential flow dynamics introduced by TMBF provides a very good approximation to the "Dry Potential" dynamics. For comparison with the results of TMBF, we adopt an aspect ratio of $A = 0.276$.

B. Linearized dynamics

Linearization of the momentum equations (1)–(3) with respect to the basic state of (4) and (5) yields

$$\frac{D_L u'}{Dt} = 2\overline{\Omega} v' - \frac{1}{\rho}\frac{\partial p'}{\partial r}, \tag{9}$$

$$\frac{D_L v'}{Dt} = -\frac{1}{\rho r}\frac{\partial p'}{\partial \theta}, \tag{10}$$

$$\frac{D_L w'}{Dt} = -\frac{1}{\rho}\frac{\partial p'}{\partial z}, \tag{11}$$

where $\frac{D_L}{Dt} = \frac{\partial}{\partial t} + \overline{\Omega}\frac{\partial}{\partial \theta}$ is the linearized material derivative.

The free surface pressure p_s is assumed to be materially conserved by the fluid parcels occupying the surface, thus $\frac{Dp_s}{Dt} = 0$. Decomposing p_s to its balanced and perturbed components, $p_s(r,\theta,z,t) = \overline{P}_s(r,z) + p'_s(r,\theta,z,t)$, this material conservation, together with (5), gives

$$\frac{Dp'_s}{Dt} = -\frac{D\overline{P}_s}{Dt} = \rho[-\overline{\Omega}^2 r u' + g w']_s, \tag{12}$$

hence under linearization

$$p'_s = \rho[-\overline{\Omega}^2 r \chi' + g\eta']_s, \tag{13}$$

in which (χ',η') are the radial and vertical displacements of the perturbed free surface, formally written in linearized form as

$$\frac{D_L \chi'}{Dt} = [u']_s, \quad \frac{D_L \eta'}{Dt} = [w']_s. \tag{14}$$

Specifically around $Z_s(L) = 0$ and $Z_s(R) = D$ we have

$$\left[p_s = -\rho\overline{\Omega}_L^2 L\chi\right]_{(L,0)}, \quad [p_s = \rho g\eta]_{(R,D)}, \tag{15}$$

where hereafter we omit the primes for perturbations. Substituting these expressions back in (10) reveals

$$\left[\frac{D_L v}{Dt} = \overline{\Omega}_L^2 \frac{\partial \chi}{\partial \theta}, \frac{D_L \chi}{Dt} = u \Rightarrow \frac{D_L^2 v}{Dt^2} = \overline{\Omega}_L^2 \frac{\partial u}{\partial \theta}\right]_{(L,0)}, \tag{16}$$

$$\left[\frac{D_L v}{Dt} = -\frac{g}{R}\frac{\partial \eta}{\partial \theta}, \frac{D_L \eta}{Dt} = w \Rightarrow \frac{D_L^2 v}{Dt^2} = -\frac{g}{R}\frac{\partial w}{\partial \theta}\right]_{(R,D)}. \tag{17}$$

III. INTERFACIAL WAVE DYNAMICS

A. Vortex sheet representation in potential flow

In the reported experiments, the swirling flow inside the container is surrounded by the ambient air. Hence, the vorticity perturbation at the interfaces can be estimated as

$$\left[(\nabla \times \mathbf{u}) \cdot \hat{\mathbf{z}} = \left(\frac{\partial (rv)}{\partial r} - \frac{1}{L}\frac{\partial u}{\partial \theta}\right)\right]_{(L,0)} = (v_f - v_a)\delta(r - L), \tag{18}$$

$$\left[(\nabla \times \mathbf{u}) \cdot \hat{\mathbf{r}} = \left(-\frac{\partial v}{\partial z} + \frac{1}{R}\frac{\partial w}{\partial \theta}\right)\right]_{(R,D)} = (v_f - v_a)\delta(z - D), \tag{19}$$

where the subscripts (f,a) represent respectively the swirling flow and the ambient air. Physically, this vorticity δ function is generated by the baroclinic torque since both the density and the pressure change abruptly across the interfaces between the flow and the ambient air (see a detailed analysis of the mechanism in Ref. [21]). The velocity far field induced by each interface can be obtained by vorticity inversion, i.e., by finding the Green function associated with those interfacial vorticity δ functions.

Under the potential flow approximation of TMBF the ambient air dynamics (v_a) is neglected, and therefore the tangential velocity perturbation (v_f) at the interface represents the vorticity δ function there. Hence, the induced velocity field by each interface can be obtained by finding the velocity potential inducing zero tangential velocity signature on the opposed interface. This is done explicitly in the next subsection.

B. Velocity splitting

We consider the perturbation velocity potential in the form of $\phi = \Phi(r,z,t)e^{im\theta}$, so that $\mathbf{v} = \nabla\phi$, and $\nabla^2\phi = 0$. Following TMBF we assume that at $(r,z) = (R,0)$ both the mass flux and the pressure are continuous. These conditions yield the normal and the tangential components of the velocity to be continuous (and not necessarily zero):

$$\left[u = \frac{\partial\phi}{\partial r}\right]_{r\to R}^{z=0} = \left[w = \frac{\partial\phi}{\partial z}\right]_{r=R}^{z\to 0}, \quad v = \left[\frac{1}{r}\frac{\partial\phi}{\partial\theta}\right]_{r\to R}^{z=0} = \left[\frac{1}{r}\frac{\partial\phi}{\partial\theta}\right]_{r=R}^{z\to 0}. \tag{20}$$

Next we decompose the potential to the parts attributed to the bottom $(L,0)$ and the top (R,D) interfacial waves, $\phi = \phi_B + \phi_T$, so that the bottom (top) wave induces zero tangential velocity at the bottom (top) one. This implies

$$\phi_{B(L,0)} = -i\frac{L}{m}v_{B(L,0)}, \quad \phi_{B(R,D)} = 0, \quad \phi_{T(L,0)} = -i\frac{R}{m}v_{T(R,D)}, \quad \phi_{T(L,0)} = 0. \tag{21}$$

The solution of the Laplace equation together with the boundary conditions of (20) and (21) yields

$$\phi_B = \frac{-i\frac{L}{m}v_{B(L,0)}}{\left[e^{\frac{-2mD}{R}}\left(\frac{L}{R}\right)^m - \left(\frac{L}{R}\right)^{-m}\right]}\begin{cases}\left[e^{\frac{-2mD}{R}}\left(\frac{r}{R}\right)^m - \left(\frac{r}{R}\right)^{-m}\right] & (L\leqslant r\leqslant R, z=0)\\ \left[e^{\frac{-2mD}{R}}e^{\frac{mz}{R}} - e^{\frac{-mz}{R}}\right] & (r=R, 0\leqslant z\leqslant D)\end{cases}, \tag{22}$$

$$\phi_T = \frac{-i\frac{R}{m}v_{T(R,D)}}{\left[e^{\frac{mD}{R}} - e^{\frac{-mD}{R}}\left(\frac{L}{R}\right)^{2m}\right]}\begin{cases}\left[\left(\frac{r}{R}\right)^m - \left(\frac{L}{R}\right)^{2m}\left(\frac{r}{R}\right)^{-m}\right] & (L\leqslant r\leqslant R, z=0)\\ \left[e^{\frac{mz}{R}} - e^{\frac{-mz}{R}}\left(\frac{L}{R}\right)^{2m}\right] & (r=R, 0\leqslant z\leqslant D)\end{cases}. \tag{23}$$

Defining

$$\alpha \equiv e^{\frac{-mD}{R}}\left(\frac{L}{R}\right)^m, \quad \beta \equiv \frac{(1+\alpha^2)}{(1-\alpha^2)}, \quad \gamma \equiv \frac{\alpha}{(1-\alpha^2)}, \tag{24}$$

then at the interfaces (22) and (23) give

$$u_{B(L,0)} = i\beta v_{B(L,0)}, \quad u_{T(L,0)} = -2i\frac{R}{L}\gamma v_{T(R,D)}, \tag{25}$$

$$w_{B(R,D)} = 2i\frac{L}{R}\gamma v_{B(L,0)}, \quad w_{T(R,D)} = -i\beta v_{T(R,D)}. \tag{26}$$

C. Interfacial wave propagation

The complete interfacial dynamics can be obtained by substituting (25) and (26) in (16) and (17):

$$\left[\frac{D_L^2 v_B}{Dt^2} = \overline{\Omega}_L^2\frac{\partial}{\partial\theta}(u_B + u_T)\right]_{(L,0)}, \quad \left[\frac{D_L^2 v_T}{Dt^2} = -\frac{g}{R}\frac{\partial}{\partial\theta}(w_B + w_T)\right]_{(R,D)}. \tag{27}$$

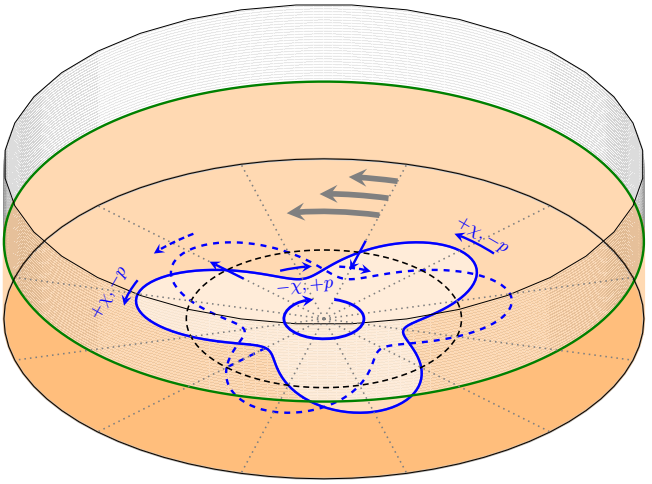

FIG. 3. Centrifugal wave counterpropagation mechanism on the cylinder horizontal surface, at the inner interface between the flow and the air. Solid lines and arrows represent the fluid displacement and velocity field at current time t, where the dashed ones represent these fields at time $(t + T/4)$ (where T is the wave period). Radial displacement is indicated by (χ) and the pressure anomaly by $(\pm p)$.

Nonetheless, the velocity splitting provides us a natural way to consider the dynamics of each interface in isolation by looking only at the self-interacting terms:

$$\left[\frac{D_L^2 v_B}{Dt^2} = \overline{\Omega}_L^2 \frac{\partial u_B}{\partial \theta}\right]_{(L,0)}, \quad \left[\frac{D_L^2 v_T}{Dt^2} = -\frac{g}{R}\frac{\partial w_T}{\partial \theta}\right]_{(R,D)}. \tag{28}$$

Assuming a wavelike solution of the form of $e^{i(m\theta-\omega t)}$, (25), (26), and (28) give the dispersion relations for the centrifugal and gravity waves:

$$\omega_c^{\pm} = m\overline{\Omega}_L\left(1 \pm \sqrt{\frac{\beta}{m}}\right), \quad \omega_g^{\pm} = m\overline{\Omega}_R\left[1 \pm \left(\sqrt{\frac{R\beta}{HFm}}\right)\right], \tag{29}$$

which are the same dispersion relations (with different notations) obtained by TMBF. The subscripts (c,g) denote the centrifugal and gravity waves, where the $(+,-)$ superscripts refer to the waves whose phase propagation is (larger, smaller) than the mean velocity at the interface.

We aim to understand the propagation mechanism of these waves, especially the centrifugal ones. Toward this end we look at their structure at the interfaces, using (15)–(17):

$$\left[(\chi, u, p)_c^{\pm} = \left(\mp\frac{1}{\overline{\Omega}_L}\sqrt{\frac{\beta}{m}}, i\beta, \pm\rho L\overline{\Omega}_L\sqrt{\frac{\beta}{m}}\right)v_c^{\pm}\right]_{(L,0)}, \tag{30}$$

$$\left[(\eta, w, p)_g^{\pm} = \left(\pm\sqrt{\frac{R\beta}{gm}}, -i\beta, \pm\rho\sqrt{\frac{Rg\beta}{m}}\right)v_g^{\pm}\right]_{(R,D)}. \tag{31}$$

In Fig. 3 we sketch the propagation mechanism of the counterpropagating centrifugal wave (c^-). As indicated from (30) the radial displacement χ and the tangential velocity v are in phase. Since outward radial displacement (positive χ) retreats the flow from the mean interface, it decreases the pressure anomaly there, hence $(\chi \propto -p \propto v)$. As discussed previously, v represents the vorticity δ function at the interface (which is positive for counterclockwise circulation) and indeed u is lagging v by a quarter of a wavelength to generate together counterclockwise rotation, in phase with χ. At the wave nodes the radial displacement, the tangential velocity and the pressure anomalies are all

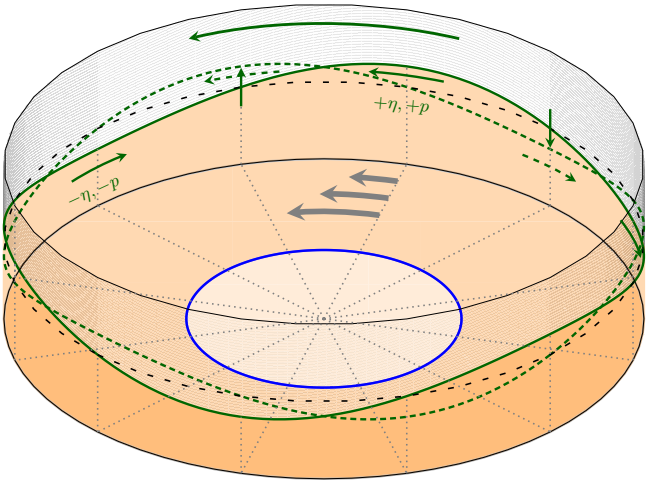

FIG. 4. Gravity wave propagation mechanism. Notations and symbols are like in Fig. 3, except that ($\pm\eta$) represents vertical wave displacement. We denote this wave as counterpropagating since it propagates counter the mean flow, measured from a frame of reference moving with the mean azimuthal mean flow.

zero. The clockwise propagation mechanism of the wave (with respect to the mean flow there which is counterclockwise) becomes intuitive now: the nonzero radial velocity u at the nodes translates the radial displacement anomalies (and hence the pressure), whereas the tangential component of the pressure gradient force at the nodes accelerates the flow, thus translating v in concert. By flipping the sign relations to ($-\chi \propto p \propto v$) it is straightforward to illustrate the propagation mechanism of the propropagating centrifugal wave (c^+). Although the gravity wave propagation mechanism is well known it is interesting to point out that it can be explained as well in a similar fashion (for more details see Ref. [20]). Figure 4 demonstrates the propagation mechanism of the counterpropagating gravity wave (g^+) where ($\eta \propto p \propto v$) at the upper interface.

IV. WAVE RESONANCE

A. Wave interaction equations

Equations (25)–(27) contain all the required information to solve the instability problem. However since each interface supports two waves, the solution by itself does not provide explicit understanding on how the four waves interact. Here we follow the method suggested by Ref. [20] to obtain explicit equations for the interfacial wave dynamics, expressed solely in terms of the waves' displacements across the interfaces.

Toward this end we express the perturbations as a sum of individually propagating interfacial waves,

$$\phi_B = \phi_c^+ + \phi_c^-, \quad \phi_T = \phi_g^+ + \phi_g^-, \quad \chi_B = \chi_c^+ + \chi_c^-, \quad \eta_T = \eta_g^+ + \eta_g^-, \tag{32}$$

where, as indicated by (30) and (31), we have

$$\left[\chi_c^\pm = \mp\left(\frac{1}{\overline{\Omega}_L}\sqrt{\frac{\beta}{m}}\right)v_c^\pm\right]_{(L,0)}, \quad \left[\eta_g^\pm = \pm\left(\sqrt{\frac{R\beta}{gm}}\right)v_g^\pm\right]_{(R,D)}. \tag{33}$$

Substituting (32) and (33) into (16) and (17) yields

$$\left[\left(\frac{\partial}{\partial t} + i\omega_c^\pm\right)\chi_c^\pm = \frac{1}{2}u_T\right]_{(L,0)}, \quad \left[\left(\frac{\partial}{\partial t} + i\omega_g^\pm\right)\eta_g^\pm = \frac{1}{2}w_B\right]_{(R,D)}. \tag{34}$$

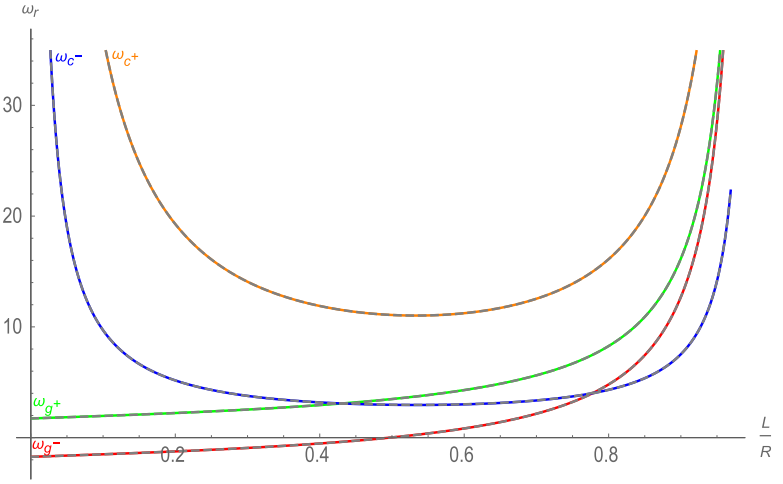

FIG. 5. The real part of dispersion relation frequencies as a function of L/R for $H/R = 0.276$ and $m = 3$. The solid gray lines are of the four branches of (ω_{NM_r}), whereas the four colored dashed lines represent the propropagating (orange) and counterpropagating (blue) centrifugal waves and the counterpropagating (green) and propropagating (red) gravity waves frequencies. All frequencies are scaled by $\sqrt{\frac{g}{R}}$ as in TMBF.

The interpretation of (34) is straightforward. Without interaction (when the RHS is zero) the intrinsic wave frequencies of (29) are recovered. With interaction, the induced far field velocity by the perturbation of a given interface is equipartitioned between the two interfacial waves at the opposed interface. Writing explicitly $[u_T]_{(L,0)}$ in terms of (η_g^+,η_g^-) and $[w_B]_{(R,D)}$ in terms of (χ_c^+,χ_c^-) we obtain

$$\left(\frac{\partial}{\partial t} + i\omega_c^{\pm}\right)\chi_c^{\pm} = -i\sigma_T(\eta_g^+ - \eta_g^-), \quad \left(\frac{\partial}{\partial t} + i\omega_g^{\pm}\right)\eta_g^{\pm} = -i\sigma_B(\chi_c^+ - \chi_c^-), \tag{35}$$

where the interaction coefficients are

$$\sigma_T \equiv \gamma\sqrt{\frac{mgR}{\beta L^2}}, \quad \sigma_B \equiv \gamma\overline{\Omega}_L\frac{L}{R}\sqrt{\frac{m}{\beta}}. \tag{36}$$

The four equations in (35) describe the explicit interaction between the four interfacial waves in terms of their local displacement at the interfaces. Substituting normal mode solutions of the form $e^{i(m\theta-\omega_{NM}t)}$ into (35) we obtain the modal dispersion relation. The real part (ω_{NM_r}) solutions are shown in Fig. 5 as a function of (L/R) at azimuthal wave number $m = 3$. The curves are identical to the ones presented in Fig. 2(a) of TMBF. The waves' frequencies without interaction $(\omega_c^{\pm},\omega_g^{\pm})$, are presented as well in this figure and nearly coincide with the corresponding normal mode frequencies. This indicates that in most regions each normal mode is dominated by the propagation of a single interfacial wave.

B. Counterpropagating wave dynamics

The positive branch of the imaginary frequency $(\omega_{NM_i} > 0)$, indicating instability, is calculated from (35) and shown in Fig. 6(a). It is identical to the one in Fig. 2(c) of TMBF. A blow-up of Fig. 5 focusing upon this region of instability is presented in Fig. 6(b), and we confirm that it is also identical to Fig. 2(b) of TMBF.

We expect that the instability results from the resonance between the waves whose intrinsic frequencies (without interaction) are close to one another. Since $\overline{\Omega}_L > \overline{\Omega}_R$, (29) suggests that those waves are of (χ_c^-,η_g^+). In the framework of the average mean frequency $\overline{\Omega}_M \equiv \frac{1}{2}(\overline{\Omega}_L + \overline{\Omega}_R)$, they

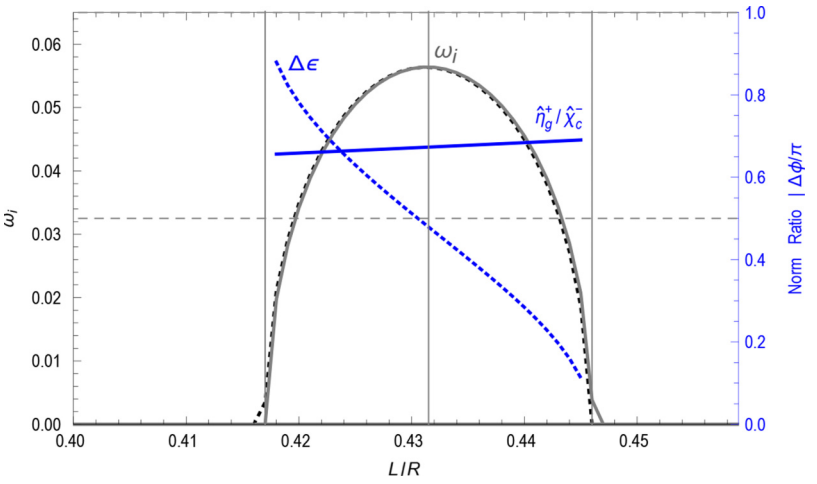

(a)

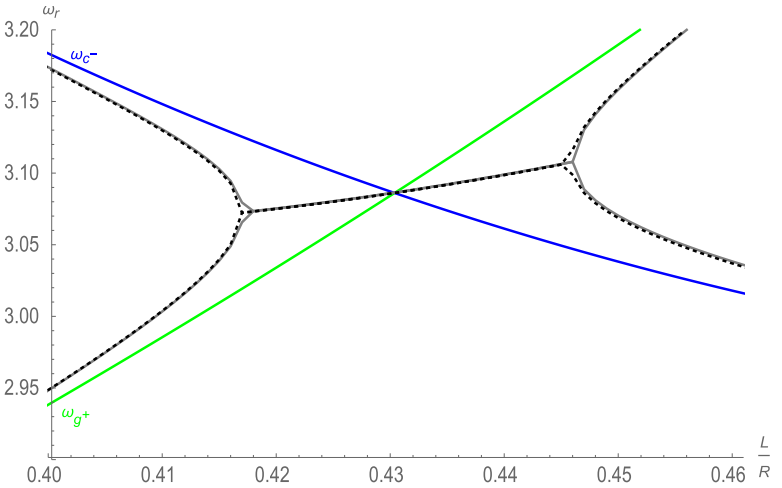

(b)

FIG. 6. Comparison between the unstable normal mode solution and the two counterpropagating waves approximation for $H/R = 0.276$ and $m = 3$. (a) The solid gray and the black dashed lines represent, respectively, the growth rate ω_{NMi} obtained from the full solution and from the two-wave system. The phase difference between the counterpropagating waves ($\Delta\epsilon = \epsilon_g^+ - \epsilon_c^-$) and their amplitude ratio ($\hat{\eta}_g^+/\hat{\chi}_c^-$) in the unstable regime is indicated by the dashed and solid blue lines, respectively. (b) Blow-up of Fig. 5 in the unstable regime. Solid gray and black dashed lines represent, respectively, ω_{NMr}, obtained from the full solution and from the two-wave system. The frequencies ω_c^- and ω_g^+ of the counterpropagation waves in isolation are indicated as well by the blue and the green solid lines.

propagate counter to their local mean flow. We therefore approximate the solution by excluding the propropagating waves (χ_c^+, η_g^-). As a result (35) is simplified to a two-wave interaction dynamics:

$$\left(\frac{\partial}{\partial t} + i\omega_c^-\right)\chi_c^- \approx -i\sigma_T \eta_g^+, \quad \left(\frac{\partial}{\partial t} + i\omega_g^+\right)\eta_g^+ \approx i\sigma_B \chi_c^-. \tag{37}$$

The two solutions of (37) are then calculated and displayed in Figs. 6(a) and 6(b). They are in a very good agreement with the full four-wave modal solution, providing nearly exact values for the

normal mode growth rates. Indeed, within the instability region, the amplitude ratios between the propropagating and the counterpropagating waves ($|\chi_c^+/\chi_c^-|, |\eta_g^-/\eta_g^+|$) are calculated and found to be less than 2% (not shown here).

Being the essential players in the instability mechanism, we wish therefore to examine more closely the nature of interaction between the counterpropagating waves. We can write the wave displacements in terms of their amplitude and phases,

$$\chi_c^- = \hat{\chi}_c^-(t)e^{i[m\theta+\epsilon_c^-(t)]}, \quad \eta_g^+ = \hat{\eta}_g^+(t)e^{i[m\theta+\epsilon_g^+(t)]} \tag{38}$$

and substitute back in (37) to obtain equations for their instantaneous growth rates and frequencies,

$$\frac{\dot{\hat{\chi}}_c^-}{\hat{\chi}_c^-} = \frac{\hat{\eta}_g^+}{\hat{\chi}_c^-}\sigma_T \sin\Delta\epsilon, \quad \frac{\dot{\hat{\eta}}_g^+}{\hat{\eta}_g^+} = \frac{\hat{\chi}_c^-}{\hat{\eta}_g^+}\sigma_B \sin\Delta\epsilon, \tag{39}$$

$$-\dot{\epsilon}_c^- = \omega_c^- + \frac{\hat{\eta}_g^+}{\hat{\chi}_c^-}\sigma_T \cos\Delta\epsilon, \quad -\dot{\epsilon}_g^+ = \omega_g^+ - \frac{\hat{\chi}_c^-}{\hat{\eta}_g^+}\sigma_B \cos\Delta\epsilon, \tag{40}$$

where $\Delta\epsilon \equiv (\epsilon_g^+ - \epsilon_c^-)$ is the displacement phase difference between the waves. In Fig. 1 the waves are sketched with a phase difference of $\Delta\epsilon = \pi/2$. As indicated by Eq. (39) this is the optimal configuration for instantaneous growth as the normal velocity, induced by each wave on the other, acts to increase the other wave's amplitude. Equation set (40) also indicates that in this configuration the wave interaction does not affect the intrinsic phase speeds of the waves. We can think of two other extreme cases, when $\Delta\epsilon = 0$ and $\Delta\epsilon = \pi$. In both cases Eq. (39) shows that the wave interaction does not lead to amplitude growth. When $\Delta\epsilon = 0$ the wave displacements are in phase but the normal velocity induced by each other are antiphased. As a result, the waves' propagation speeds are reduced, hence the waves hinder each other's propagation with respect to the mean flow. Consequently, the instantaneous frequency $-\dot{\epsilon}_c^-$, becomes more positive, whereas $-\dot{\epsilon}_g^+$, becomes more negative as a result of the interaction. When $\Delta\epsilon = \pi$ the waves are antiphased in terms of their displacement but in phase in terms of their normal velocity. This helps the wave to propagate counter the mean flow. For any phase relation in the range of $(0 < \Delta\epsilon < \pi/2)$ the wave interaction makes the amplitudes to grow and hinder the counterpropagation rate. In the range of $(\pi/2 < \Delta\epsilon < \pi)$ the waves amplify each other and help each other to counterpropagate against the average mean flow.

C. Normal modes instability in terms of counterpropagating wave resonance

Normal mode are the solutions of Eqs. (39) and (40), where, by definition, both waves experience the same growth rate (ω_{NMi}) and are phase-locked to propagate with the same frequency (ω_{NMr}):

$$\omega_{NMi} = \frac{\dot{\hat{\chi}}_c^-}{\hat{\chi}_c^-} = \frac{\dot{\hat{\eta}}_g^+}{\hat{\eta}_g^+}, \quad \omega_{NMr} = -\dot{\epsilon}_c^- = -\dot{\epsilon}_g^+. \tag{41}$$

These requirements determine the waves' amplitude ratio and phase difference:

$$\frac{\hat{\eta}_g^+}{\hat{\chi}_c^-} = \sqrt{\frac{\sigma_B}{\sigma_T}}, \quad \cos\Delta\epsilon = \frac{\omega_g^+ - \omega_c^-}{2\sqrt{\sigma_B\sigma_T}} \tag{42}$$

as well as the explicit expressions for the normal mode growth rate and propagation frequency (Fig. 6):

$$\omega_{NMi} = \tfrac{1}{2}\sqrt{[4\sigma_B\sigma_T - (\omega_g^+ - \omega_c^-)^2]}, \quad \omega_{NMr} = \tfrac{1}{2}(\omega_g^+ + \omega_c^-). \tag{43}$$

The phase difference ($\Delta\epsilon = (\epsilon_g^+ - \epsilon_c^-)$) and amplitude ratio ($\hat{\eta}_g^+/\hat{\chi}_c^-$) are plotted in Fig. 6(a). We can explicitly see how the region of instability is bounded by the ability of the waves to be phase-locked to form a growing normal mode with mutual wave amplification. The mean frequency ratio $\overline{\Omega}_R/\overline{\Omega}_L = (L/R)^2 < 1$. Hence, for small (L/R) ratio the difference between the mean flow

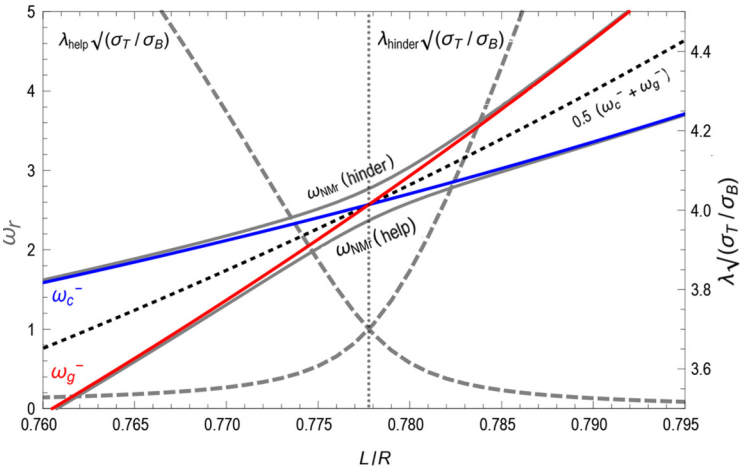

FIG. 7. Interaction of counter- and propropagating waves which result in neutral normal modes, for $H/R = 0.276$ and $m = 3$. (a) The two modal frequencies (gray lines) for which the waves hinder or help the other to propagate. The wave frequencies in isolation [ω_c^- (blue), ω_g^- (red)] and their averaged values $(\omega_c^- + \omega_g^-)/2$ (doted line) are shown as well for comparison. Plotted as dashed lines are the scaled amplitude ratio $(\sqrt{\frac{\sigma_T}{\sigma_B}}\lambda)$ for the helping and hindering solutions of Eq. (50) (right axis for corresponding values).

phase speeds are relatively large thus the wave should help each other to counterpropagate against the shear to remain phase-locked ($\pi > \Delta\epsilon > \pi/2$). As the ratio (L/R) becomes closer to unity the difference between Ω_R and Ω_L decreases and the waves should hinder each other's phase propagation to remain phase-locked ($\pi/2 > \Delta\epsilon > 0$), where the margins of instability are obtained when $\Delta\epsilon = (0,\pi)$. The most unstable mode is manifested when the phase difference is almost at $\Delta\epsilon = 0.48\pi \approx \pi/2$, which is very near the optimal configuration for instantaneous growth when $\omega_g^+ = \omega_c^-$.

The amplitude ratio for the most unstable mode ($\hat{\eta}_g^+/\hat{\chi}_c^- = 0.67$). However, since both $L/D < 1$ and $L/R < 1$, the visual effect of this amplitude ratio may diminish the actual amplitude ratio even more.

D. The near resonance regime

Equation set (37), together with the understanding of the wave propagation and interaction mechanisms, indicate that instantaneous amplification is possible either between a pair of two counterpropagating waves (χ_c^-,η_g^+), or between a pair of two propropagating waves (χ_c^+,η_g^-). Obviously, as was shown in the previous subsection, out of the two pairs only the growth between the counterpropagating ones can be sustained to form modal structure with exponential growth. Nevertheless one can obtain neutral normal modes, which are composed off a combination of a counter- and a propropagating wave. This is the case described in Fig. 7 which includes the information of Fig. 2(d) in TMBF. The interaction is between the waves of (χ_c^-,η_g^-), so that relatively to the shear the centrifugal wave χ_c^- is counterpropagating whereas $\hat{\eta}_g^-$ is propropagating. The waves are phase-locked to propagate in concert either when they help each other propagation when their amplitudes are in phase ($\Delta\epsilon = \epsilon_g^- - \epsilon_c^- = 0$) [Figs. 8(a) and 8(b)], or when their amplitudes are in antiphased ($\Delta\epsilon = \pi$) [Figs. 8(c) and 8(d)] when they hinder each other. Since the self-propagation rate of both waves is clockwise (i.e., negative) "helping" will decrease the phased-locked frequency and "hindering" will increase it. The difference in the helping and hindering scenarios is in the amplitude ratio between the two waves. At any rate since the waves are neutral their structure will not emerge in the rotating tank experience. For completeness, however, we present here the analysis of this neutral "near resonance" interaction.

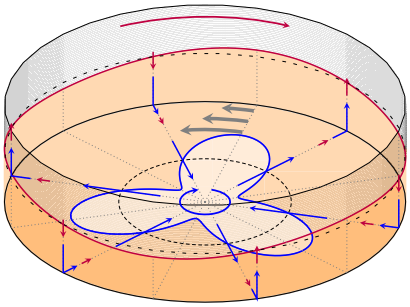

(a)

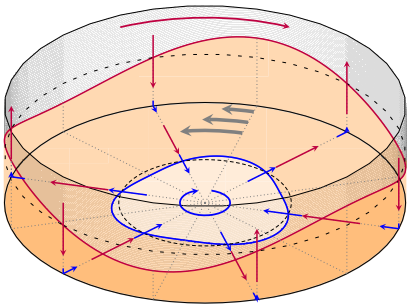

(b)

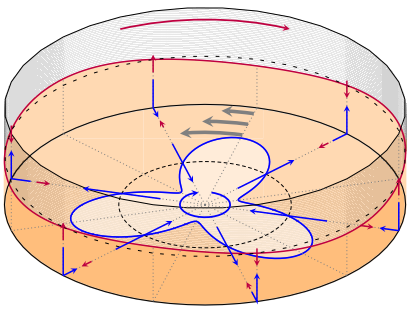

(c)

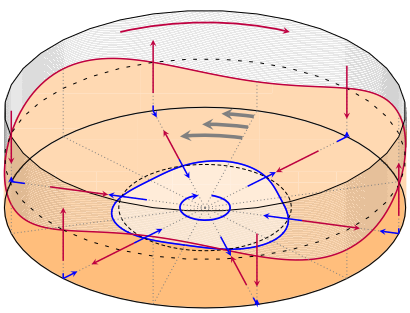

(d)

FIG. 8. The "near resonance" interaction between the waves of (χ_c^-, η_g^-). The waves help each other to propagate when (a) $\hat{\chi}_c^- > \hat{\eta}_g^-$ for $L/R < 0.778$ or when (b) $\hat{\chi}_c^- < \hat{\eta}_g^-$ for $L/R > 0.778$. The waves hinder each other to propagate when (c) $\hat{\chi}_c^- > \hat{\eta}_g^-$ for $L/R > 0.778$ or when (d) $\hat{\chi}_c^- < \hat{\eta}_g^-$ for $L/R < 0.778$.

Writing

$$\chi_c^- = \hat{\chi}_c^-(t)e^{i[m\theta+\epsilon_c^-(t)]}, \quad \eta_g^- = \hat{\eta}_g^-(t)e^{i[m\theta+\epsilon_g^-(t)]}, \tag{44}$$

and approximating (35) to

$$\left(\frac{\partial}{\partial t} + i\omega_c^-\right)\chi_c^- \approx i\sigma_T\eta_g^-, \quad \left(\frac{\partial}{\partial t} + i\omega_g^-\right)\eta_g^- \approx i\sigma_B\chi_c^-, \tag{45}$$

the real parts of (45) can be written as

$$\frac{\dot{\hat{\chi}}_c^-}{\hat{\chi}_c^-} = -\frac{\hat{\eta}_g^-}{\hat{\chi}_c^-}\sigma_T \sin\Delta\epsilon, \quad \frac{\dot{\hat{\eta}}_g^-}{\hat{\eta}_g^-} = \frac{\hat{\chi}_c^-}{\hat{\eta}_g^-}\sigma_B \sin\Delta\epsilon. \tag{46}$$

Hence the only modal solution is of zero growth rate:

$$\omega_{NMi} = \frac{\dot{\hat{\chi}}_c^-}{\hat{\chi}_c^-} = \frac{\dot{\hat{\eta}}_g^-}{\hat{\eta}_g^-} = 0, \tag{47}$$

yielding $\Delta\epsilon = (0,\pi)$. The imaginary parts of (45) become

$$-\dot{\epsilon}_c^- = \omega_c^- - \frac{\hat{\eta}_g^-}{\hat{\chi}_c^-}\sigma_T\cos\Delta\epsilon, \quad -\dot{\epsilon}_g^- = \omega_g^- - \frac{\hat{\chi}_c^-}{\hat{\eta}_g^-}\sigma_B\cos\Delta\epsilon, \tag{48}$$

thus for modal solution, $\omega_{NMr} = -\dot{\epsilon}_c^- = -\dot{\epsilon}_g^+$,

$$\Delta\omega = \pm\left(\sigma_T\lambda - \frac{\sigma_B}{\lambda}\right), \tag{49}$$

with the frequency difference $\Delta\omega \equiv (\omega_c^- - \omega_g^-)$ and amplitude ratio $\lambda \equiv \hat{\eta}_g^-/\hat{\chi}_c^-$. The plus solution corresponds to $\Delta\epsilon = 0$, i.e., the "helping" solution, whereas the minus corresponds to the $\Delta\epsilon = \pi$, "hindering" one. This gives the amplitude ratio solution:

$$\lambda_{(\text{help,hinder})} = \frac{\pm\Delta\omega + \sqrt{(\Delta\omega)^2 + 4\sigma_T\sigma_B}}{2\sigma_T}, \tag{50}$$

corresponding to

$$\omega_{NMr(\text{help,hinder})} = \frac{1}{2}(\omega_c^- + \omega_g^-) \mp \frac{\sqrt{\sigma_T\sigma_B}}{2}\left[\left(\sqrt{\frac{\sigma_T}{\sigma_B}}\lambda\right) + \left(\sqrt{\frac{\sigma_T}{\sigma_B}}\lambda\right)^{-1}\right]. \tag{51}$$

These two modal frequencies are plotted in Fig. 7 together with ω_c^-, ω_g^-, $(\omega_c^- + \omega_g^-)/2$ and the two solutions of $(\sqrt{\frac{\sigma_T}{\sigma_B}}\lambda)$; $\Delta\omega > 0$ at $L/R < 0.778$ and $\Delta\omega < 0$ at $L/R > 0.778$. For $\Delta\omega > 0$ phase locking can be achieved when the waves help each other to propagate if $\hat{\eta}_g^- > \hat{\chi}_c^-$ [Fig. 8(b)]. Then the g^- wave affects the c^- one more than vice versa, thus g^- helps c^- to propagate more than c^- helps g^-. The result is that g^- enforces c^- to propagate with a frequency which is even smaller than ω_g^- since the c^- decreases by little the wave propagation frequency of g^- (recall that the self-propagation rate of each wave in isolation is clockwise, i.e., negative). Consequently the phase-locked normal mode frequency $\omega_{NMhelp} < \omega_g^-$ (but still positive due to the advection of the mean flow). The other option for phase locking for $\Delta\omega > 0$ is that the waves hinder each other and $\hat{\chi}_c^- > \hat{\eta}_g^-$ [Fig. 8(c)]. Then c^- slows (thus makes the frequency more positive) g^- more than vice versa and enforces g^- to propagate with a frequency which is even larger than ω_c^- as the g^- increases by little the wave propagation speed of c^-. Consequently the phase-locked normal mode frequency $\omega_{NMhinder} > \omega_c^-$ (taking the advection of the mean flow as well into the account). When $\Delta\omega < 0$ at $L/R > 0.778$ the roles between the two waves are switched. The helping and hindering configurations for this case are plotted in Figs. 8(a) and 8(d), respectively.

V. SUMMARY

The aim of this study is to provide a physical understanding for the propagation mechanism of the inner surface centrifugal waves, as well as for the mechanism by which they interact in a distance with the outer vertical gravity waves to form resonance instability. This work follows the analysis presented in the first part of TMBF. It might be therefore useful to summarize the results in the current paper with respect to TMBF. TMBF have managed to reduce substantially the complexity of the problem by considering the elegant quasi-2D potential flow model. They obtained the complex modal dispersion relation for the four eigenvalues of the system. They found two regions of interest of unstable and stable wave interaction dynamics, where the interactions are between four waves; two are the familiar outer gravity waves and the other two were coined as centrifugal surface waves. TMBF derived as well the dispersion relation of each of the four waves in isolation and showed mathematically how the Cairns condition [23] for instability is satisfied in the unstable region but not in the stable one. Nonetheless, several basic questions remained open. What is the physical propagation mechanism of the centrifugal waves and why can they propagate in two opposite directions with respect to the local mean flow? How do the inner horizontal centrifugal waves and the outer vertical gravity waves interact in a distance? Specifically, the four waves have different intrinsic phase speeds, while under a modal solution all waves propagate at the same phase speed. Thus, how does the interaction in a distance mutually affect the waves' phase speeds (either attenuates or amplifies them)? Furthermore, modal instability is obtained when all of the four waves experience the same growth rate. Now, each wave is neutral in isolation, hence, how does the interaction between the waves yield such mutual growth rate? Understanding that, why does it work in the unstable regime but not in the stable one?

In order to answer these questions we first decomposed the velocity field attributed by the four waves (Sec. III B) to study the interfacial wave propagation in isolation (Sec. III C). It was found that the centrifugal waves are a potential flow representation of baroclinic edge waves, where the sharp gradients of density and pressure across the fluid-air interface yield baroclinic torques that generate a wavy vortex sheet at the edge (which, in principle, is the same wave propagation mechanism discussed in Ref. [21]). With respect to the local mean flow the waves intrinsic frequencies are such that they propagate in the (counter-) clockwise direction when the vertical component of their vorticity anomalies are (in) antiphase with the wave radial displacement (Fig. 3 demonstrates the clockwise propagation mechanism including the role played by the tangential pressure gradient force perturbation).

In the quasi-2D model the waves interact in a distance by transforming the horizontal surface flux to the vertical outward flux and vice versa. Therefore, the radial velocity induced by the surface centrifugal waves is converted into vertical velocity in the water tank walls which affects the vertical gravity waves. Similarly, downward motion induced by those vertical gravity waves is transformed to radial motion that affects back the surface centrifugal waves. As is illustrated in Fig. 1 a pair of centrifugal and gravity waves can amplify each others' amplitude displacement when they are in quadrature (out of phase by a quarter of wavelength). Nonetheless, a mutual amplification that may lead to instability is possible only between a pair of waves whose intrinsic phase speeds are in opposite directions (that is, either the centrifugal wave propagates counterclockwise and the gravity wave clockwise, or vice versa). The waves may also amplify (attenuate) each others' intrinsic phase speeds when the cross-stream velocity induced by one wave on the other are in (anti) phase, Figs. 8(a) and 8(b) [Figs. 8(c) and 8(d)]. This way, despite the mean shear, the waves can lock themselves to propagate with the same modal frequency. Furthermore, resonance instability can be obtained only if the locking is between counterpropagating waves, which are the clockwise centrifugal wave and the counterclockwise gravity wave.

These mechanisms of wave interaction are expressed mathematically in Eq. (35). The reduction from the four wave interaction dynamics to only two counterpropagating wave interaction [Eqs. (37)–(40) provide the essence of the general setups that may lead to growth, including nonmodal transient growth, which is not discussed here]. The normal mode dispersion relation obtained by

TMBF is then analyzed in terms of the wave interaction dynamics. The modal instability is related to the ability of the two counterpropagating waves to exhibit the same growth rate and to be phase-locked with the same phase speed [Eqs. (41) and (43)]. Furthermore, the stability regime found by TMBF is studied in details as well in Sec. IV D. It is shown that the fundamental difference between the two regimes is that the interaction in the stable regime is obtained between pairs of pro- and counter propagating waves which cannot mutually amplify each other but only to phase lock each other in a neutral configuration.

The vorticity wave interaction approach has been applied this far to resonant instability between Rossby [19], gravity [22], capillary [24], and even Alfvén waves in shear dynamics of plasma [25]. Hence, it is our aim to analyze the other resonant instability mechanisms obtained in swirling flow experiments with lower rotation rates, where both Rossby and inertial waves participate in the resonant instability mechanism.

ACKNOWLEDGMENT

E.H. is grateful to Tomas Bohr for showing him the experience of fast rotating swirling flow in his laboratory in DTU.

[1] G. H. Vatistas, A note on liquid vortex sloshing and Kelvin's equilibria, J. Fluid Mech. **217**, 241 (1990).
[2] G. H. Vatistas, J. Wang, and S. Lin, Experiments on waves induced in the hollow core of vortices, Exp. Fluids **13**, 377 (1992).
[3] T. R. N Jansson, M. P. Haspang, K. H. Jensen, P. Hersen, and T. Bohr, Polygons on a Rotating Fluid Surface, Phys. Rev. Lett. **96**, 174502 (2006).
[4] T. Suzuki, M. Iima, and Y. Hayase, Surface switching of rotating fluid in a cylinder, Phys. Fluids **18**, 101701 (2006).
[5] G. H. Vatistas, H. A. Abderrahmane, and M. H. K. Siddiqui, Experimental Confirmation of Kelvin's Equilibria, Phys. Rev. Lett. **100**, 174503 (2008).
[6] Y. Tasaka and M. Iima, Flow transitions in the surface switching of rotating fluid, J. Fluid Mech. **636**, 475 (2009).
[7] R. Bergmann, L. Tophøj, T. A. M. Homan, P. Hersen, A. Andersen, and T. Bohr, Polygon formation and surface flow on a rotating fluid surface, J. Fluid Mech. **679**, 415 (2011).
[8] R. Bergmann, L. Tophoj, T. A. M. Homan, P. Hersen, A. Andersen, and T. Bohr, Polygon formation and surface flow on a rotating fluid surface—Erratum, J. Fluid Mech. **691**, 605 (2012).
[9] A. Mandour, M. Fayed, H. Ait Abderrahmane, H. D. Ng, L. Kadem, and G. H. Vatistas, Symmetry-breaking of interfacial polygonal patterns and synchronization of travelling waves within a hollow-core vortex, Chaotic Model. Simul. **1**, 256 (2012).
[10] H. A. Abderrahmane, M. Fayed, H. D. Ng, and G. H. Vatistas, A note on relative equilibria in a rotating shallow water layer, J. Fluid Mech. **724**, 695 (2013).
[11] B. Bach, E. C. Linnartz, M. H. Vested, A. Andersen, and T. Bohr, From Newton's bucket to rotating polygons: Experiments on surface instabilities in swirling flows, J. Fluid Mech. **759**, 386 (2014).
[12] J. Mougel, D. Fabre, and L. Lacaze, Waves in Newton's bucket, J. Fluid Mech. **783**, 211 (2015).
[13] D. Fabre and J. Mougel, Generation of three-dimensional patterns through wave interaction in a model of free surface swirling flow, Fluid Dyn. Res. **46**, 061415 (2014).
[14] J. Mougel, D. Fabre, and L. Lacaze, Waves and instabilities in rotating free surface flows, Mech. Ind. **15**, 107 (2014).
[15] L. Tophøj, J. Mougel, T. Bohr, and D. Fabre, Rotating Polygon Instability of a Swirling Free Surface Flow, Phys. Rev. Lett. **110**, 194502 (2013).
[16] M. Amaouche, H. A. Abderrahmane, and G. H. Vatistas, Nonlinear modes in the hollow-cores of liquid vortices, Eur. J. Mech. B Fluids **41**, 133 (2013).
[17] B. J. Hoskins, M. E. McIntyre, and A. W. Robertson, On the use and significance of isentropic potential vorticity maps, Q. J. R. Meteorol. Soc. **111**, 877 (1985).

[18] P. G. Baines and H. Mitsudera, On the mechanism of shear flow instabilities, J. Fluid Mech. **276**, 327 (1994).

[19] E. Heifetz, C. H. Bishop, and P. Alpert, Counter-propagating Rossby waves in the barotropic Rayleigh model of shear instability, Q. J. R. Meteorol. Soc. **125**, 2835 (1999).

[20] N. Harnik, E. Heifetz, O. M. Umurhan, and F. Lott, A buoyancy-vorticity wave interaction approach to stratified shear flow, J. Atmos. Sci. **65**, 2615 (2008).

[21] E. Heifetz and J. Mak, Stratified shear flow instabilities in the non-Boussinesq regime, Phys. Fluids **27**, 086601 (2015).

[22] J. R. Carpenter, E. W. Tedford, E. Heifetz, and G. A. Lawrence, Instability in stratified shear flow: Review of a physical interpretation based on interacting waves, Appl. Mech. Rev. **64**, 060801 (2011).

[23] R. A. Cairns, The role of negative energy waves in some instabilities of parallel flows, J. Fluid Mech. **92**, 1 (1979).

[24] L. Biancofiore, F. Gallaire, and E. Heifetz, Interaction between counterpropagating Rossby waves and capillary waves in planar shear flows, Phys. Fluids **27**, 044104 (2015).

[25] E. Heifetz, J. Mak, J. Nycander, and O. M. Umurhan, Interacting vorticity waves as an instability mechanism for magnetohydrodynamic shear instabilities, J. Fluid Mech. **767**, 199 (2015).